PHYSICAL REVIEW B **71**, 245321 (2005)

Contact block reduction method for ballistic transport and carrier densities of open nanostructures

D. Mamaluy and D. Vasileska
Department of Electrical Engineering, Center for Solid State Electronics Research,
Arizona State University, Tempe, Arizona 85287-5706

M. Sabathil, T. Zibold, and P. Vogl
Walter Schottky Institute, Technische Universitaet Muenchen, 85748 Garching, Germany

(Received 15 July 2004; revised manuscript received 18 March 2005; published 23 June 2005)

A method is presented for quantum-mechanical ballistic transport calculations of realistic two- and three-dimensional open devices that may have any shape and any number of leads. Observables of the open system can be calculated with an effort comparable to a single calculation of a suitably defined closed system. The method is based on a previously developed scheme for calculating transmission functions, the contact block reduction method, and is shown to be applicable to the density matrix, the density of states, and the local carrier density. The electronic system may be characterized by a single or multiband Hamiltonian. We illustrate the method for the four-band GaAs hole transport through a two-dimensional three-terminal T-junction device and for the electron tunneling through a three-dimensional InAs quantum dot molecule embedded into an InP heterostructure.

DOI: 10.1103/PhysRevB.71.245321 PACS number(s): 73.63.Kv, 73.23.−b

I. INTRODUCTION

With the recent advances in semiconductor technology it became possible to fabricate nanodevices with dimensions less than the mean free path and the dephasing length, so that ballistic transport effects dominate the overall device behavior. These devices include very different structures, such as nano-MOSFETs, modulation doped 2DEGs, resonant tunneling devices, etc. Simultaneously to the progress of the experimental fabrication and characterization techniques, significant effort has been dedicated to the theoretical prediction of the transport properties of such open quantum systems.

The most widely used scheme to calculate the ballistic transport through an open system is the Landauer-Buttiker formalism.[1,2] With this method, the current is calculated from the transmission function that is obtained from the solution of the Schrödinger equation with scattering boundary conditions. While this is a significant simplification compared to a calculation that includes the relaxation of carriers, even this approach becomes computationally very challenging for higher dimensional nanostructures with a complex geometry.

Several methods have been developed to calculate the ballistic transport through quantum devices. A well-known approach is the transfer matrix method.[3,4] While this scheme has been found to become unstable[5] for larger devices in its original form, this drawback has been overcome by a series of generalizations developed by Frensley,[6,7] Lent *et al.*,[8] and Ting *et al.*[9,10] These approaches use the quantum transmitting boundary method[8] (QTBM) to account for the coupling to the leads, and can handle structures of arbitrary geometry. The price to be paid, however, is that the size of the linear systems that need to be solved repeatedly is of the order of the area or the volume of the entire device. Therefore, published implementations of the QTBM still appear to be limited to one-dimensional tight-binding[9,11,12] or $k\cdot p$ based[10] multiband calculations, or two-dimensional (2D) single-band calculations.[8,13] Recently, a three-dimensional self-consistent scheme has been published[14] that is applicable to quasi-two-dimensional structures. However, this approach is limited to separable problems and single band Hamiltonians. The boundary element method[15] is computationally more efficient, but so far the published applications are limited to waveguide structures, i.e., structures possessing a flat potential[16] or consisting of piecewise homogeneous materials with constant potentials.[17] Another efficient and widely used algorithm is the recursive Green's function method[18,19] that has been successfully implemented for two-dimensional devices[20,21] and for small three-dimensional structures such as nanowires.[22] It is very well suited for two-terminal devices that can be discretized into cross-sectional slices with nearest neighbor interactions but has difficulties dealing with additional contacts that inevitably couple more distant slices with one another. A closely related modular recursive Green's function method[23] is applicable to devices that can be divided into regions of sufficiently high symmetry, where the Schrödinger equation is separable, and has been recently adopted to include magnetic fields.[24] Very recently, a modified version of the QTBM has been developed that expands the scattering solutions in terms of two different closed system wave functions in an efficient way.[25] This scheme is charge self-consistent and has been implemented for single-band situations so far. Thus, the quantum-mechanical ballistic multiband transport calculation of large two- and three-dimensional structures or devices with more than two Ohmic contacts still presents a significant challenge.

In this work, we present an efficient Green's function method to calculate the electronic properties of open quantum systems such as the transmission, the density of states, and the carrier density in the ballistic limit. The presently developed scheme is applicable to multiterminal two- and three-dimensional structures without geometric constraints and can handle single and as well as multiband $\mathbf{k}\cdot\mathbf{p}$ or tight-binding Hamiltonians. The method rests on a Green's function approach that rigorously separates the open system problem into the single solution of a suitably defined closed system and the repeated solution of a small linear system of equations of size determined by the contact regions that couple the closed system to the leads. We have termed this method the contact block reduction method (CBR) in an earlier paper that focused solely on the calculation of the ballistic transmission function. We show in this paper that the calculation of the charge density of the open system throughout the device can be performed with an effort comparable to a single calculation of a small percentage of the eigenstates of a closed system.

This paper is organized as follows. In Sec. II a brief summary of the CBR method in terms of the Green's function formalism is provided. A general expression for the density matrix of an open system in terms of the eigenstates of the corresponding closed system is derived in Sec. III. The generalization of the method to multiband Hamiltonians is presented in Sec. IV. A further significant reduction of the computational effort can be achieved for the special case of single band Hamiltonians by transforming the basis into the space of propagating modes of the leads, as it is shown in Sec. V. In Secs. VI and VII, respectively, we present two numerical examples. We predict the hole conductance in a GaAs based T-junction device and the resonant current through an InAs quantum dot molecule that is embedded within InP barrier material. These examples highlight the applicability of the CBR method to multiband $\mathbf{k}\cdot\mathbf{p}$ Hamiltonians and realistic three-dimensional devices.

II. GREEN'S FUNCTIONS FOR OPEN DEVICES

In this section we briefly review the key ingredients of the contact block reduction method[28] and set up the notation that is used throughout the paper. We consider a system that consists of some n-dimensional ($n=1$, 2, 3) region that we term "device" and an arbitrary number of leads that couple the device to reservoirs. The device may be under applied bias and contain some spatially varying potential. The total Hamiltonian operator of the system, including the device and the leads, can be written in the symbolic matrix form

$$H_{\text{tot}} = \begin{pmatrix} H_1 & 0 & 0 & W_1 \\ 0 & \ddots & 0 & \vdots \\ 0 & 0 & H_L & W_L \\ W_1^\dagger & \cdots & W_L^\dagger & H^0 \end{pmatrix}, \qquad (1)$$

where H_λ represents the Hamiltonian of lead λ, the Hamiltonian H^0 corresponds to the device region, and W_λ is the coupling between the device and this lead ($\lambda=1,\ldots,L$). The leads (acting as reservoirs) are semi-infinite and, therefore, the total Hamiltonian H_{tot} is infinite dimensional. Since we are interested in ballistic transport of electrons through the finite device region, it is convenient to describe the device including its coupling to the leads in the following manner.[26] It is represented by a finite effective (non-Hermitian) Hamiltonian $H=H^0+\Sigma$ of the *open device*, where the influence of the external leads is included through a finite-dimensional operator Σ that can be derived from Eq. (1) as will be explained below. The Hermitian Hamiltonian H^0 represents, by contrast, a closed system, i.e., the device with no coupling to the leads or *decoupled device*. We assume throughout this work that the Hamiltonian H does not contain scattering terms. In this ballistic case, all observables of interest can, in principle, be obtained from the retarded Green's function G^R of the open device, which is defined by

$$G^R = (E-H)^{-1} = (E-H^0-\Sigma)^{-1}, \qquad (2)$$

where $\Sigma=\Sigma_1+\Sigma_2+\cdots+\Sigma_L$, and Σ_λ represents the complex self-energy due to the coupling W_λ between lead λ and the device. We can express Eq. (2) in terms of the Green's function G^0 of the decoupled device in the following manner:

$$G^R = (1-G^0\Sigma)^{-1}G^0,$$

$$G^0 = (E-H^0+i\eta)^{-1}, \quad \eta\to 0+. \qquad (3)$$

The Green's function G^0 can also be expressed in terms of the eigenstates $|\alpha\rangle$ of the decoupled device Hamiltonian H^0 as follows:

$$G^0 = \sum_\alpha \frac{|\alpha\rangle\langle\alpha|}{E-\varepsilon_\alpha+i\eta}, \quad \eta\to 0+,$$

$$H^0|\alpha\rangle = \varepsilon_\alpha|\alpha\rangle. \qquad (4)$$

Contact block reduction formalism

The evaluation of the retarded Green's function in Eq. (2) requires the inversion of a large matrix that is proportional to the number of grid points or cells of the device,[6,8,27] which can be quite demanding even in two spatial dimensions. The essence of the contact block reduction method consists in the decomposition of G^R into blocks such that the transmission function of the open device can be calculated by inverting only small matrices.[28]

The first step in this procedure is to choose a real space discretization of the device region and subdivide the total grid space of N_T points into N_L boundary grid points that overlap with the leads—*contacts*—and the interior region with $N_D=N_T-N_L$ points. Typically the number N_T exceeds N_L by several orders of magnitude. The real space Hamiltonian matrix that corresponds to this discretization is assumed to couple only sites within some finite range with one another, typically only nearest neighbors. The contact grid points associated with lead λ form the set C_λ of all points where the coupling matrix W_λ in Eq. (1) is nonzero. The number of grid points in this set that links the device with the lead λ is denoted by N_λ. The total number N_L of boundary grid points that overlap with leads is given by

$$N_L = \sum_{\lambda=1}^{L} N_\lambda. \qquad (5)$$

It is convenient to number the grid points, denoted by letters $i,j,k,l,\ldots$, in such a way that the total grid space is given by the following ordered set:

$$\Omega = \{C_1 \cup C_2 \cup \cdots C_L\} \cup \{D = \text{interior part of device}\}. \tag{6}$$

The self-energy in Eq. (2) reflects the coupling of the device to the leads and is given by the expression[26]

$$\boldsymbol{\Sigma}_\lambda(i,j) = \begin{cases} (\mathbf{W}_\lambda \mathbf{G}_\lambda^R \mathbf{W}_\lambda^\dagger)_{ij}, & i,j \in C_\lambda, \\ \mathbf{0}, & i,j \notin C_\lambda, \end{cases} \tag{7}$$

where $\boldsymbol{\Sigma}_\lambda$ and $\mathbf{G}_\lambda^R$ are the self-energy matrix and the retarded Green's function matrix of lead λ, respectively. Note that we indicate all real space representations of operators, i.e., matrices, by bold letters. In the basis of the ordered set, Eq. (6), the total self-energy matrix $\boldsymbol{\Sigma}$ is given by a block-diagonal matrix of the form

$$\boldsymbol{\Sigma} = \begin{pmatrix} \boldsymbol{\Sigma}_C & \mathbf{0} \\ \mathbf{0} & \mathbf{0}_D \end{pmatrix}, \tag{8}$$

$$\boldsymbol{\Sigma}_C = \boldsymbol{\Sigma}_1 \oplus \boldsymbol{\Sigma}_2 \oplus \cdots \boldsymbol{\Sigma}_L. \tag{9}$$

The submatrix $\boldsymbol{\Sigma}_C$ is of dimension N_L and $\mathbf{0}_D$ is a square null submatrix of dimension N_D associated with the interior part of the device. In addition, we define the Hermitian matrix

$$\boldsymbol{\Gamma} = i(\boldsymbol{\Sigma} - \boldsymbol{\Sigma}^\dagger), \tag{10}$$

which has the same structure as the self-energy matrix. Analogously, we define $\mathbf{G}_C^R$ to be the submatrix of the open device's retarded Green's function $\mathbf{G}^R$ within the contact regions. Now, let us write the Dyson equation [Eq. (3)] for $\mathbf{G}^R$ in matrix form,

$$\mathbf{G}^R = [\mathbf{1} - \mathbf{G}^0\boldsymbol{\Sigma}]^{-1}\mathbf{G}^0 = \mathbf{A}^{-1}\mathbf{G}^0, \tag{11}$$

$$\mathbf{A} = \mathbf{1} - \mathbf{G}^0\boldsymbol{\Sigma}. \tag{12}$$

We now subdivide the matrix $\mathbf{G}^0$ into blocks corresponding to the contact portion $\mathbf{G}_C^0$ and the interior device portion $\mathbf{G}_D^0$, in analogy to the self-energy matrix defined in Eq. (8). Then,

$$\mathbf{G}^0 = \begin{bmatrix} \mathbf{G}_C^0 & \mathbf{G}_{CD}^0 \\ \mathbf{G}_{DC}^0 & \mathbf{G}_D^0 \end{bmatrix}. \tag{13}$$

Note that $\mathbf{G}_C^0$ is a small matrix of size N_L, in contrast to $\mathbf{G}_D^0$ which has size $N_D \gg N_L$. Similarly, we subdivide the matrix $\mathbf{A}$ into blocks which leads to

$$\mathbf{A} = \begin{bmatrix} \mathbf{1}_C - \mathbf{G}_C^0\boldsymbol{\Sigma}_C & \mathbf{0} \\ -\mathbf{G}_{DC}^0\boldsymbol{\Sigma}_C & \mathbf{1}_D \end{bmatrix}. \tag{14}$$

Here, the submatrix $\mathbf{A}_C = \mathbf{1} - \mathbf{G}_C^0\boldsymbol{\Sigma}_C$ is a square matrix of dimension N_L, whereas the lower diagonal block of $\mathbf{A}$ is a square unit matrix of dimension N_D. The inverse of the full matrix $\mathbf{A}$ possesses exactly the same structure as $\mathbf{A}$ itself, namely

$$\mathbf{A}^{-1} = \begin{bmatrix} \mathbf{A}_C^{-1} & \mathbf{0} \\ \mathbf{G}_{DC}^0\boldsymbol{\Sigma}_C\mathbf{A}_C^{-1} & \mathbf{1}_D \end{bmatrix}. \tag{15}$$

Using this result Eq. (15) and Eq. (11), the full retarded Green's function of the open device can be finally written as

$$\mathbf{G}^R = \begin{bmatrix} \mathbf{A}_C^{-1}\mathbf{G}_C^0 & \mathbf{A}_C^{-1}\mathbf{G}_{CD}^0 \\ \mathbf{G}_{DC}^0\boldsymbol{\Sigma}_C\mathbf{A}_C^{-1}\mathbf{G}_C^0 + \mathbf{G}_{DC}^0 & \mathbf{G}_{DC}^0\boldsymbol{\Sigma}_C\mathbf{A}_C^{-1}\mathbf{G}_{CD}^0 + \mathbf{G}_D^0 \end{bmatrix}. \tag{16}$$

This important relation shows that *any* block of $\mathbf{G}^R$ can be calculated by inverting only the small submatrix $\mathbf{A}_C$. Based on this result, it is now easy to show[28] that the transmission and the reflection function can be entirely expressed in terms of the small submatrix $\mathbf{G}_C^R = \mathbf{A}_C^{-1}\mathbf{G}_C^0$,

$$T_{\lambda\lambda'}(E) = \mathrm{Tr}(\boldsymbol{\Gamma}_C^\lambda \mathbf{G}_C^R \boldsymbol{\Gamma}_C^{\lambda'} \mathbf{G}_C^{R\dagger}), \quad \lambda \neq \lambda' \tag{17}$$

$$T_{\lambda\lambda}(E) = R_\lambda(E) = \mathrm{Tr}[(\mathbf{1}_C^\lambda - i\boldsymbol{\Gamma}_C^\lambda \mathbf{G}_C^R)(\mathbf{1}_C^\lambda - i\boldsymbol{\Gamma}_C^\lambda \mathbf{G}_C^R)^\dagger], \tag{18}$$

$$\boldsymbol{\Gamma}_C^\lambda = i(\boldsymbol{\Sigma}_C^\lambda - \boldsymbol{\Sigma}_C^{\lambda\dagger}). \tag{19}$$

The contact elements of the decoupled Green's function $\mathbf{G}_C^0$ are to be determined through the spectral representation given in Eq. (4).

III. CONTACT BLOCK REDUCTION METHOD FOR THE DENSITY MATRIX

In this section we show that the CBR method can be extended to observables that are functions of the carrier density in a way that maintains the advantages and the computational efficiency of this scheme. This generalization is a prequisite for charge self-consistent calculations. The results presented in this section apply equally well to single-band and multiband $\mathbf{k}\cdot\mathbf{P}$ or tight-binding Hamiltonians. The only assumption we make is that the basis is localized in real space so that nearest-neighbor interactions provide an adequate representation of the Hamiltonian matrix.

In order to derive a general expression for the density matrix, we first consider the spectral function $\mathbf{S}$ of the open device that is defined by[26]

$$\mathbf{S} \equiv \mathbf{G}^R\boldsymbol{\Gamma}\mathbf{G}^{R\dagger}. \tag{20}$$

Since $\boldsymbol{\Gamma}$ in Eq. (10) is nonzero only within the contact region, $\mathbf{S}$ can be written as

$$\mathbf{S} = \begin{pmatrix} \mathbf{G}_C^R & \mathbf{G}_{CD}^R \\ \mathbf{G}_{DC}^R & \mathbf{G}_D^R \end{pmatrix} \begin{pmatrix} \boldsymbol{\Gamma}_C & \mathbf{0} \\ \mathbf{0} & \mathbf{0} \end{pmatrix} \begin{pmatrix} \mathbf{G}_C^{R\dagger} & \mathbf{G}_{DC}^{R\dagger} \\ \mathbf{G}_{CD}^{R\dagger} & \mathbf{G}_D^{R\dagger} \end{pmatrix} \tag{21}$$

$$= \begin{pmatrix} \mathbf{G}_C^R\boldsymbol{\Gamma}_C\mathbf{G}_C^{R\dagger} & \mathbf{G}_C^R\boldsymbol{\Gamma}_C\mathbf{G}_{DC}^{R\dagger} \\ \mathbf{G}_{DC}^R\boldsymbol{\Gamma}_C\mathbf{G}_C^{R\dagger} & \mathbf{G}_{DC}^R\boldsymbol{\Gamma}_C\mathbf{G}_{DC}^{R\dagger} \end{pmatrix}. \tag{22}$$

This matrix consists of four blocks that may be denoted by $\mathbf{S}_{XX'}$ with elements $X, X' \in \{C, D\}$. One can easily see that the left column of the matrix in Eq. (16) can be expressed in the form[29]

$$\mathbf{G}_{XC}^R = \mathbf{G}_{XC}^0\mathbf{B}_C^{-1},$$

$$\mathbf{B}_C \equiv \mathbf{1}_C - \boldsymbol{\Sigma}_C\mathbf{G}_C^0, \tag{23}$$

where again $X \in \{C, D\}$. Inserting this into Eq. (21) leads to the following expression for the spectral function:

$$\mathbf{S}_{XX'} = \mathbf{G}^0_{XC}\mathbf{B}_C^{-1}\mathbf{\Gamma}_C(\mathbf{B}_C^{-1})^\dagger(\mathbf{G}^0_{X'C})^\dagger. \tag{24}$$

Using spectral representations for the decoupled Green's functions $\mathbf{G}^0_{XC}$, Eq. (4), we can rewrite the matrix elements of $\mathbf{S}$ in terms of the discrete real space basis as follows:

$$\begin{aligned}\mathbf{S}_{ij} &= \sum_{k,l\in C}\left(\sum_\alpha \frac{\langle i|\alpha\rangle\langle\alpha|k\rangle}{(E-\varepsilon_a+i\eta)}\right)\\ &\quad\times[\mathbf{B}_C^{-1}\mathbf{\Gamma}_C(\mathbf{B}_C^{-1})^\dagger]_{kl}\left(\sum_\beta \frac{\langle l|\beta\rangle\langle\beta|j\rangle}{(E-\varepsilon_a-i\eta)}\right)\Bigg]_{\eta\to 0+}\\ &= 2\pi\sum_{\alpha,\beta}\langle i|\alpha\rangle\langle\beta|j\rangle\Xi_{\alpha\beta}(E),\end{aligned} \tag{25}$$

$$\Xi_{\alpha\beta}(E) = \frac{1}{2\pi}\left.\frac{\mathrm{Tr}\{[|\beta\rangle\langle\alpha|]_C\mathbf{B}_C^{-1}\mathbf{\Gamma}_C\mathbf{B}_C^{-1\dagger}\}}{(E-\varepsilon_a+i\eta)(E-\varepsilon_\beta-i\eta)}\right|_{\eta\to 0+}. \tag{26}$$

Equation (25) for the spectral function is our starting point for the derivations of the characteristics of the open system, such as the local density of states, the density matrix, and the charge density. Note that this expression only contains the inverse of the small matrix $\mathbf{B}_C$ of size N_L that is associated with the contact-device coupling. The term $\Xi_{\alpha\beta}(E)$ plays the role of a generalized density of states of the open system and is expressed in terms of the eigenstates $|\alpha\rangle, |\beta\rangle$ of the decoupled device, i.e., the closed system. In the limiting case of $\mathbf{\Gamma}_C \to 0$ (closed system), one gets $\Xi_{\alpha\beta}(E)=\delta_{\alpha\beta}\delta(E-E_\alpha)$ as shown in Appendix A. The local density of states $\rho_i(E) = (1/2\pi)S_{ii}(E)$ at grid point i follows now from

$$\rho_i(E) = \sum_{\alpha,\beta}\langle i|\alpha\rangle\langle\beta|i\rangle\Xi_{\alpha\beta}(E). \tag{27}$$

By integrating this expression over real space, the density of states is obtained as

$$N(E) = \mathrm{Tr}\,\Xi(E). \tag{28}$$

Finally, we can express the density in terms of $\Xi_{\alpha\beta}(E)$. The device is connected to L leads that represent particle reservoirs in local equilibrium and are characterized by lead distribution functions $f_\lambda(E), \lambda=1,\ldots,L$. It has been shown before that the particle density of an open system can be expressed for such a situation in the form[27,30]

$$n_i = \frac{1}{2\pi}\int dE\sum_{\lambda=1}^{L} f_\lambda(E)\langle i|\mathbf{G}^R\mathbf{\Gamma}^\lambda\mathbf{G}^{R\dagger}|i\rangle, \tag{29}$$

where $\mathbf{\Gamma}^\lambda$ is the matrix defined in Eq. (10) with self-energies associated with lead λ. Note that a direct calculation of this expression would involve the solution of a very large linear system of equations. Using the contact block reduction method and the results given by Eq. (25), by contrast, yields a computationally efficient expression for the particle density n_i,

$$n_i = \sum_{\alpha,\beta}\langle i|\alpha\rangle\langle\beta|i\rangle\boldsymbol{\xi}_{\alpha\beta}, \tag{30}$$

$$\boldsymbol{\xi}_{\alpha\beta} = \sum_{\lambda=1}^{L}\int \Xi^\lambda_{\alpha\beta}(E)f_\lambda(E)dE, \tag{31}$$

where $\boldsymbol{\xi}_{\alpha\beta}$ is the density matrix, and the matrix $\Xi^\lambda_{\alpha\beta}$ is defined analogously to Eq. (26), with $\mathbf{\Gamma}_C$ being replaced by $\mathbf{\Gamma}^\lambda_C$ as defined in Eq. (19).

Numerical details and computational costs: The CBR method expresses the problem of ballistic scattering through an open nanostructure in terms of those parts of the retarded Green's function that connect the contacts to the interior device. Here we assess the numerical cost of calculating the density or local density of states in this approach. All of the matrices involved in Eq. (26) are of small size $N_L \times N_L$. Initially, we solve the Hermitian eigenvalue problem for the decoupled device which requires $O(N_T N^2_{\mathrm{eigen}})$ operations for N_{eigen} eigenstates, $N_{\mathrm{eigen}} \leqslant N_T$. The cost for the calculation of the transmission function[28] given by Eq. (17) is $N_E \times [O(N_L^3) + N_L^2 N_{\mathrm{eigen}}]$, where N_E is the number of energy grid points. The calculation of the local density of states in Eq. (27) or the particle density n_i requires $N_{\mathrm{CBR}} = N_E \times N_L^2 N^2_{\mathrm{eigen}} + N_T N^2_{\mathrm{eigen}}$ operations, since the matrix elements of $\Xi_{\alpha\beta}(E)$ need to be calculated only once for all grid points i. As we will show below, it suffices for a mesoscopic device to calculate only a few percent of all N_T eigenvalues so that $N_{\mathrm{CBR}} \leqslant N_E N_T$. This leads to a dramatic additional reduction in computer time.

IV. MULTIBAND LEAD MODE DISPERSION AND SELF-ENERGY

In this section, we set up a concrete model for the self-energy Eq. (7) that couples the device to the leads, taking into account a general multiband Hamiltonian and a two- or three-dimensional device. Several ballistic lead models have been proposed. A recently published paper[22] treats the lead of a three-dimensional device as infinitely extended bulk in the two directions parallel to the contact surface so that the lead eigenstates are two-dimensional plane waves. In this paper, we adopt the more common approach[26] to treat the lead as a semi-infinite straight quantum wire of finite circumference. For the following discussion, we pick out an individual lead of that type and calculate its self-energy. It is convenient to express it in terms of the eigenmodes $\chi(y,z)$ of an infinitely extended and homogeneous quantum wire. These modes propagate along the wire direction $\hat{z}$ and are confined states in the perpendicular directions. All cross-sectional coordinates including band indices are lumped into the index y. With these assumptions, the wire modes are product states of one-dimensional plane waves along the lead wire and cross-sectional localized wave functions that are independent of the position z, i.e.,

$$\chi(y,z) = e^{ikz}\psi(y). \tag{32}$$

Let us discretize the quantum wire by introducing cross-sectional slices at positions $z=la$, where $l=0,\pm 1,\pm 2,\ldots$ is an integer and a is the grid spacing. To keep the notation simple, we only include nearest-neighbor coupling in the Hamiltonian. We adopt a vector notation so that the wire

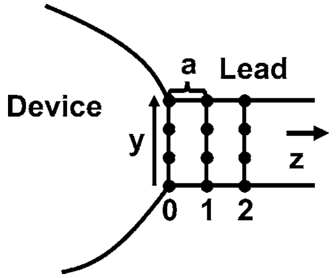

FIG. 1. Schematic picture of local coordinate system of an individual semi-infinite lead attached to the device. The dots indicate the two- or three-dimensional discrete grid points. Along the lead axis z, the lattice spacing is a. The origin of the z axis lies at the contact boundary.

eigenfunctions $\chi(y,z)$ are replaced by vectors χ_l of dimension M, where M cycles through all degrees of freedom except the position l along the wire. These wave functions obey the Schrödinger equation,

$$(\mathbf{H}_{l,l}-E\mathbf{1})\chi_l+\mathbf{W}^{\dagger}\chi_{l-1}+\mathbf{W}\chi_{l+1}=0, \qquad (33)$$

where the matrix $\mathbf{H}_{l,l}$ is the cross-sectional part of the wire Hamiltonian, and $\mathbf{W}$ denotes the coupling between adjacent slices. To simplify notation and without loss of generality, we assume here the coupling constant between the lead slices to be the same as between the contact slice of the device and the lead. Note that $\mathbf{H}_{l,l}$ is the same for all slices l and is set up in such a way that the wave functions vanish at the circumference of the quantum wire. By employing the Bloch condition $\chi_l=\exp(ik_\mu a)\chi_{l-1}$, Eq. (33) can be rewritten in the form of a non-Hermitian linear eigenvalue problem for the complex wire band structure $k_\mu(E)$ and the wire eigenfunctions χ_l^μ,

$$\begin{pmatrix}(\mathbf{H}_{l,l}-E\mathbf{1}) & \mathbf{W}\\ \mathbf{1} & \mathbf{0}\end{pmatrix}\begin{pmatrix}\chi_l\\ \chi_{l+1}\end{pmatrix}_\mu=e^{-ik_\mu a}\begin{pmatrix}-\mathbf{W}^{\dagger} & \mathbf{0}\\ \mathbf{0} & \mathbf{1}\end{pmatrix}\begin{pmatrix}\chi_l\\ \chi_{l+1}\end{pmatrix}_\mu. \qquad (34)$$

The solution of Eq. (34) yields the wire mode dispersion $k_\mu(E)$ of the $2M$ linearly independent modes χ_l^μ which are propagating or decaying to the right and to the left, respectively. Now we consider the semi-infinite lead that extends from the contact at $l=0$ to $l\to+\infty$ (see Fig. 1).

The self-energy couples the device with this semi-infinite lead and can be expressed in terms of those M modes χ_l^μ that propagate or decay into the leads ($l\to+\infty$). Within these M modes, the evanescent ones have $\mathrm{Im}(k_\mu)<0$ whereas the propagating ones are characterized by $\mathrm{Im}(k_\mu)=0$ and group velocity $v_g^\mu>0$. The latter can be calculated from[12]

$$v_g^\mu(E)=-\frac{2a}{\hbar|\chi_l^\mu|^2}\mathrm{Im}[(\chi_l^\mu)^{\dagger}\mathbf{W}^{\dagger}\chi_l^\mu e^{ik_\mu a}], \qquad (35)$$

which is independent of l. Finally, the self-energy can be written in the following form:[22]

$$\mathbf{\Sigma}_C=-\mathbf{W}\mathbf{K}^{-1}\mathbf{\Lambda}\mathbf{K}, \qquad (36)$$

where $\mathbf{K}$ is the $M\times M$ matrix of the column vectors χ_0^μ at the contact site ($l=0$), and $\mathbf{\Lambda}$ is a diagonal matrix,

$$\mathbf{\Lambda}=\mathrm{diag}\{\exp[-ik_1(E)a],\ldots,\exp[-ik_M(E)a]\}. \qquad (37)$$

We note that the wire dispersion relation can be solved analytically if the wire Hamiltonian describes either a single energy band or decoupled bands. In that case, the Hamiltonian is separable and has the form

$$H_L(y,z)=H_\perp(y)+T_\parallel(z), \qquad (38)$$

where $H_\perp$ is the cross-sectional lead Hamiltonian that obeys a 1D or 2D Schrödinger equation

$$H_\perp|\psi^\mu\rangle=\varepsilon^\mu|\psi^\mu\rangle, \qquad (39)$$

and the term $T_\parallel$ represents the kinetic energy along the propagation direction. In addition, in this case, the coupling matrix $\mathbf{W}$ in Eq. (36) is proportional to the unit matrix, $\mathbf{W}=W\mathbf{1}$. This gives the following expression for the self-energy Σ at a contact:[26]

$$\mathbf{\Sigma}_C(i,j)=-W\sum_{\mu}^{M}\langle i|\psi^\mu\rangle\exp(ik^\mu a)\langle\psi^\mu|j\rangle \quad (i,j\in C_\lambda), \qquad (40)$$

where the wire dispersion $k^\mu(E)$ is given analytically by the relation

$$E=\varepsilon^\mu+2W[1-\cos(k^\mu a)]. \qquad (41)$$

Thus, the cross-sectional lead modes must be calculated only once in the single band case.

Boundary condition for device Hamiltonian: The splitting of the Hamiltonian H into a decoupled device Hamiltonian H^0 and the self-energy Σ is not unique. This degree of freedom can be exploited such that the low-lying eigenstates of H^0 mimic the scattering states of the open system which greatly reduces the effort to calculate the retarded Green's function of the open device.[28] If we simply truncate the infinite system's Hamiltonian right at the contacts to define H^0, we obtain the self-energy as given by Eq. (36). This corresponds to Dirichlet (i.e., infinite barrier) boundary conditions for H^0. For single-band Hamiltonians, we have found previously that it is significantly more efficient to include the energy-independent part of the self-energy into H^0 and to redefine the self-energy correspondingly. This procedure is equivalent to applying von Neumann boundary conditions to H^0 at the contacts. In this section, we generalize this procedure to multiband Hamiltonians.

By using a formal series expansion of the exponents, we decompose the diagonal matrix $\mathbf{\Lambda}$ for an individual lead into the unit matrix plus an energy-dependent term,

$$\mathbf{\Lambda}(E)=\mathbf{1}+\mathbf{\Lambda}'(E),$$

$$\mathbf{\Lambda}'=\mathrm{diag}\{\exp[-ik_1(E)a]-1,\ldots,\exp[-ik_M(E)a]-1\}. \qquad (42)$$

We substitute this back into the self-energy to get

$$\mathbf{\Sigma}_C = -\mathbf{W} - \mathbf{W}\mathbf{K}^{-1}\mathbf{\Lambda}'\mathbf{K}. \tag{43}$$

Since $\mathbf{W}$ is not Hermitian, we symmetrize it as

$$\mathbf{W}^H = \tfrac{1}{2}(\mathbf{W} + \mathbf{W}^\dagger), \tag{44}$$

and redefine the decoupled device Hamiltonian and the self-energy, respectively, as

$$\mathbf{H}^N = \mathbf{H}^0 - \mathbf{W}^H, \tag{45}$$

$$\mathbf{\Sigma}_C^N = \mathbf{\Sigma}_C + \mathbf{W}^H. \tag{46}$$

The multiband Hamiltonian $\mathbf{H}^N$ corresponds to a closed system with generalized von Neumann boundary conditions at the contact boundaries. Thus, the eigenfunctions of the Hamiltonian $\mathbf{H}^N$ are approximate solutions of the open-boundary problem in the low energy limit.[28] As a consequence, by solving the Dyson equation [Eq. (3)] with $\mathbf{H}^N$ instead of $\mathbf{H}^0$, it suffices to include an incomplete set of eigenfunctions in the spectral representation of $\mathbf{H}^N$ for some limited energy range. From a numerical point of view, this is the most crucial time-saving step in the CBR method that will be illustrated in Sec. VI.

V. MODE SPACE REDUCTION IN SINGLE-BAND CASE

In this section, we show that the numerical effort of calculating the transmission function and the density matrix of the open system can be further reduced in the single-band case by transforming the Green's functions and the self-energy into a basis of propagating mode states. Since the cross-sectional mode eigenfunctions ψ^μ of a given lead in Eq. (40) are orthogonal and complete, we can transform the real space matrices $\mathbf{G}^0_{C,ij}, \mathbf{\Sigma}_{C,ij}$, and $\mathbf{\Gamma}_{C,ij}$ into mode space, where the indices i,j are elements of the contact set C. This leads to diagonal matrices $\mathbf{\Sigma}_{\mu\mu}$ (and $\mathbf{\Gamma}_{\mu\mu}$) and full matrices $\mathbf{G}^0_{\mu\nu}$ with (greek) mode indices μ,ν,

$$\mathbf{\Sigma}_{C,\mu\mu} = \sum_{i,j\in C} \langle \psi^\mu | i \rangle \mathbf{\Sigma}_{C,ij} \langle j | \psi^\mu \rangle = -W \exp(ik^\mu a), \tag{47}$$

$$\mathbf{G}^0_{C,\mu\nu} = \sum_{i,j\in C} \langle \psi^\mu | i \rangle \mathbf{G}^0_{C,ij} \langle j | \psi^\nu \rangle. \tag{48}$$

Correspondingly, one has $\mathbf{\Gamma}_{\mu\mu} = 2\,\mathrm{Im}\,\mathbf{\Sigma}_{C,\mu\mu}$. Therefore, the purely real elements $\mathbf{\Sigma}_{C,\mu\mu}$ correspond to $\mathbf{\Gamma}_{\mu\mu}=0$ and do not contribute to the traces in the transmission function given by Eq. (17) and the density matrix determined from Eq. (26), because they correspond to decaying modes. In contrast to the transmission, the Green's function of the open device $\mathbf{G}^R$ is determined, in principle, by the full self-energy $\mathbf{\Sigma}_C$ including purely real elements.[31] Here we show, however, that the error introduced by neglecting the decaying modes in the calculation of $\mathbf{G}^R$ is negligible. Generally speaking, this is a consequence of lateral momentum conservation or, equivalently, matching between lead and device modes. We write Eq. (48) in terms of the eigenstates $|\alpha\rangle$ of the Hermitian Hamiltonian H^N,

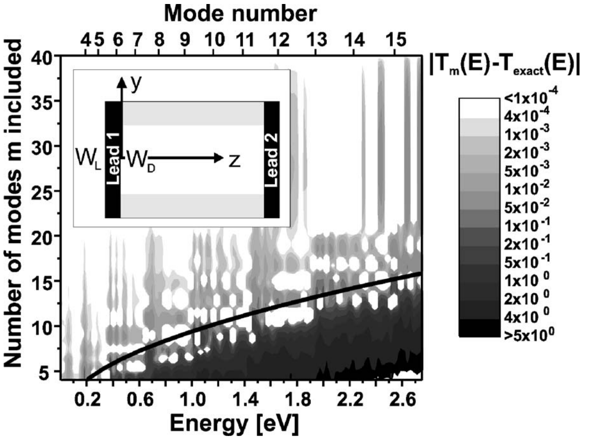

FIG. 2. Contour plot of the difference between the exact and mode truncated transmission function for the device shown in the inset. The parameters used are W_D=5 nm, W_L=10 nm, L=10 nm, m^*=0.3 m_0, and a constant grid spacing of 0.167 nm. The total number of modes is M=61.

$$G^0_{C,\mu\nu} = \sum_\alpha \frac{\langle \psi^\mu | \alpha \rangle \langle \alpha | \psi^\nu \rangle}{E - E^N_\alpha + i\eta}. \tag{49}$$

Assume for a moment that the leads and the device are laterally planar, infinitely extended heterostructures. Then, both the lead states $|\psi^\nu\rangle, |\psi^\mu\rangle$ and the eigenstates $|\alpha\rangle$ of the decoupled system are eigenfunctions of the lateral momentum and the matrix $G^0_{C,\mu\nu}(E)$ is diagonal. This strict conservation law gets softened gradually for leads of finite diameter as we will discuss below; it becomes invalid only for extremely narrow leads but then the matrix $G^0_{C,ij}$ is already of small size in real space and no transformation to mode space is necessary.

We will illustrate the effect of mode matching by a simple example. Consider a two-dimensional two-terminal device of width W_D in the interior of the device and length L as schematically illustrated in the inset of Fig. 2. The two leads may have a width W_L that can be larger or smaller than W_D (Fig. 2 shows the situation $W_L > W_D$). The grey-shaded areas inside the device represent impenetrable barriers, and the interior potential is considered to be constant. For the arguments given below, only the potential near the contacts matters. Since devices are usually designed to have flat potentials near contacts, this model mimics realistic situations at least qualitatively.

Assume first that $W_L = W_D$. In that case, the cross-sectional lead and device states are trivially orthogonal to each other so that only a single mode contributes to the sum in Eq. (49) and the matrix $G^0_{C,\mu\nu}(E)$ is diagonal again. Now consider the more realistic situation $W_L \neq W_D$ and we first study the situation $W_L > W_D$ as depicted in the inset of Fig. 2. This figure depicts a contour plot of the difference in magnitude between the exactly calculated transmission function $T_{12,\text{exact}}(E)$ [see Eq. (17)] and the truncated transmission function $T_{12,m}(E)$. The latter includes only a fixed number $m \leq M$ of lead modes in the matrix $G^0_{\mu\nu}$ in Eq. (48) and the Dyson equation Eq. (11). The horizontal axis shows the energy, and the number of modes included in $T_m(E)$ is plotted along the vertical axis.

The thick line marks the border line between the propagating and the decaying lead modes. As one can see, the neglect of all decaying lead modes leads only to an error of the order of 0.1% in the transmission coefficient. For this simple device, the difference in the transmission functions between the two leads as shown in Fig. 2 equals the corresponding difference in the reflection functions of one lead, $|R_{1,\mathrm{exact}}(E)-R_{1,m}(E)+m-M|$. In Appendix C, we are analyzing this simple box device analytically and evaluate the matrix elements of $G^{0}_{\mu\nu}$ for modes μ,ν belonging to the same lead. This analysis makes it clear that the dominant matrix elements $\langle\psi^{\mu}|\alpha\rangle$ in Eq. (49) are those that correspond to propagating lead states since the decaying ones are poorly matched and almost orthogonal to the device states.

We have additionally analyzed this device for the situation where $W_L < W_D$. This must be done numerically since the two-dimensional eigenstates of the open device are no longer separable into one-dimensional ones in this case. We find that for $W_L/W_D < 0.5$, the error in the transmission due to the neglect of all but the propagating lead states is of the order of 10%. It suffices, however, to include a few decaying states in addition to the propagating lead states in order to obtain well converged results.

These results grossly reduce the numerical effort in calculating the inverse of the matrix $\mathbf{B}_C$ as defined in Eq. (23). Similarly, the density in Eq. (29) can be calculated efficiently by employing a mixed real space/mode representation for $\mathbf{G}_R$.

VI. ASSESSMENT OF MULTIBAND CBR METHOD: HOLE TRANSPORT IN T-SHAPED JUNCTION

The efficiency of the CBR method for the fully quantum mechanical calculation of the transmission function, the density of states, and the carrier density, as developed in this paper, rests on three key points: (i) the evaluation of all of theses observables requires only that part of the retarded Green's function $\mathbf{G}^R$ that connects the contacts to the interior device; (ii) $\mathbf{G}^R$ can be evaluated efficiently by calculating only a few percent of the eigenstates of a suitably defined Hermitian Hamiltonian $\mathbf{H}^N$, Eq. (45); (iii) for single-band Hamiltonians, the size of the contact part of the $\mathbf{G}^R$ matrix can be grossly reduced by transforming into the basis of all propagating lead modes which amount to only a few percent of all modes.

To illustrate the applicability of the method in the multiband case, we consider a T-junction that is formed by two crossing GaAs quantum wells. Such a device can be realized by the cleaved edge overgrowth technique[32] and has been investigated experimentally extensively.[33–37] However, the complicated geometry has hampered realistic theoretical studies on transport properties so far.[38,39]

To be concrete, we assume the barrier material to be p-doped and analyze the ballistic quantum transport characteristics of holes in the GaAs wells. We assume the two perpendicular GaAs quantum wells to be embedded within $\mathrm{Al}_{0.3}\mathrm{Ga}_{0.7}\mathrm{As}$ barrier material. One quantum well consists of a 6 nm thick GaAs layer that is grown along the [100] direction. After cleavage along the [011] surface, a second quantum well of 4 nm thickness is grown, followed by a cap layer of $\mathrm{Al}_{0.3}\mathrm{Ga}_{0.7}\mathrm{As}$ (see Fig. 3).

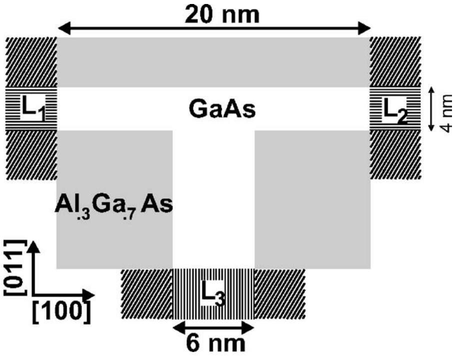

FIG. 3. Sketch of the T-junction device used in the calculation. The leads are indicated by the patterned regions.

Since this device possesses three contacts, it is not possible to reduce the problem size to one-dimensional slicing, which is a prerequisite for the recursive Green's function method.[18] We have discretized the two-dimensional structure shown in Fig. 3, using a 20 nm by 20 nm mesh with constant grid spacing of 0.5 nm. The leads are indicated by the striped regions and labeled L_1 to L_3. Since the valence band offset (barrier height) is only 140 meV, the transverse wave functions of the leads penetrate into the barrier regions (indicated by the diagonal stripes) in Fig. 3. Therefore, the diameter of the semi-infinite lead wires must be considerably larger than the quantum well thickness such that the wire modes are completely decayed at the wire boundaries. We employ a four band $\mathbf{k}\cdot\mathbf{p}$ Hamiltonian (see Appendix B) to calculate the band structure for the holes. The Hamiltonian includes the $p_{3/2}$ spinor states and couples the light and heavy hole bands but neglects the $p_{1/2}$ states. With the exception of the valence band offset, the $\mathbf{k}\cdot\mathbf{p}$ parameters are taken to be the same throughout the structure.

The strong coupling between heavy and light hole bands induced by the lateral confinement results in a complicated dispersion function in the leads that must be evaluated numerically at each energy step. We first analyze the properties of the leads—such as dispersion and group velocity—for the case of zero wave vector along the free $k_{[01\bar{1}]}$ direction and then perform the integration over k space along the $[01\bar{1}]$ direction to obtain the conductance and the local carrier density.

A. Lead dispersion

For the first lead L_1 (see Fig. 3), the quantization axis lies parallel to [100], whereas the propagation direction is [011]. Figure 4 shows the dispersion $k_{[011]}(E)$, and the corresponding group velocity $v_g(E)$ for this lead. The pronounced quantization strongly mixes the heavy and light holes. Some propagating modes only exist within a certain energy interval and then decay, leading to the maxima and semiparabolas in the group velocity. Thus, the number of propagating modes is no longer monotonously rising with increasing energy as is the case for parabolic bands.

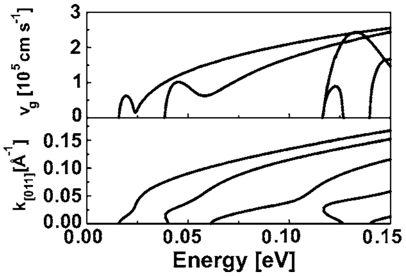

FIG. 4. Lower box, subband structure of the lead L_1. Energy is in eV, the wave vector k lies along the [011] direction. Upper box, corresponding group velocity in 10^5 cm/s as a function of energy in each band. The perpendicular wave vector along $[01\bar{1}]$ has been set equal to zero.

The second lead L_2 (see Fig. 3) is quantized in the [011] direction, and the carriers propagate along the [100] direction. Figure 5 shows the dispersion $k_{[100]}(E)$, and the corresponding group velocity. As in lead L_1, the bands are strongly coupled, but exhibit a slightly higher group velocity due to the smaller effective mass in the [100] direction. The third lead L_3 has identical properties, as is obvious from Fig. 4.

It is interesting to note that the onset of the first propagating mode occurs at almost the same energy for the L_1 and L_2 leads in spite of their different width of 6 and 4 nm, respectively. This is due to the highly anisotropic mass of the heavy hole band that reaches its maximum along the [011] direction. This result would not be obtained in a single-band analysis with parabolic masses which would lead to incorrect transmission characteristics.

B. Transmission function and density of states

Using the CBR method, the transmission function between the three leads can be calculated very efficiently. The transmission function $T(E)$ shown in Fig. 6 is a spiky function due to the reflections caused by the sharp edges in the T-junction potential. The density of states provides information regarding the total number of carriers in the device and is depicted in Fig. 7.

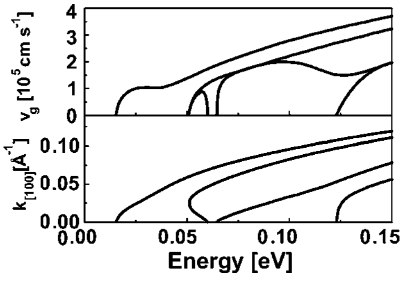

FIG. 5. Lower box, subband structure of the lead L_2. Energy is in eV, the wave vector k lies along the [100] direction. Upper box, corresponding group velocity in 10^5 cm/s as a function of energy in each band. The perpendicular wave vector along $[01\bar{1}]$ has been set equal to zero.

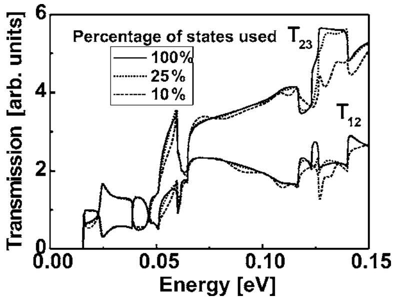

FIG. 6. The transmission functions $T_{12}(E)=T_{13}(E)$ and $T_{23}(E)$ of the T-junction, plotted as a function of energy in eV. The perpendicular wave vector along $[01\bar{1}]$ has been set equal to zero. The exact calculations (solid curves) are compared to results with a reduced set of eigenstates, either using 25% (dashed curves) or using 10% (dotted curves) of all eigenstates.

As we have pointed out in Sec. IV, we compute the decoupled Green function by employing a transformation that corresponds to generalized von Neumann boundary conditions. We performed a series of calculations that included either all or only a fraction of the eigenstates of H^N in the spectral representation of G^0. Figure 6 compares the transmission functions T_{12} and T_{23} calculated exactly (solid lines) with those obtained by including only a subset of eigenstates, namely the lowest 25 (dashed lines) or 10% (dotted lines) of all states. This reduction corresponds to cutoff energies of 1.5 and 0.6 eV, respectively. As one can deduce from Figs. 6 and 7, the inclusion of 25% of the eigenstates still guarantees basically exact results for low energies.

Thus, the reduction of the problem size that can be achieved by neglecting high energy eigenstates in G^0 is comparable for multiband Hamiltonians and for single-band Hamiltonians,[28] although the strong coupling between the bands requires a higher cutoff energy in the former case.

C. Conductance

So far, we only presented auxiliary quantities such as transmission and density of states. In this section, we present concrete predictions of the conductance for the T-junction shown in Fig. 3. So far, no experimental data on this structure seem to be available; however, hole transport in AlGaAs

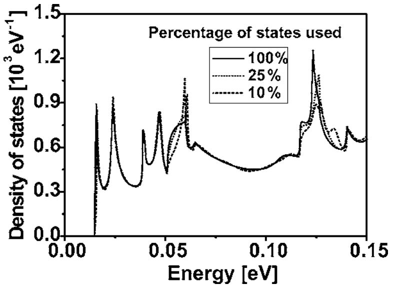

FIG. 7. Density of states of the T-junction in units of 10^3 eV^{-1} as a function of energy in eV. The perpendicular wave vector along $[01\bar{1}]$ has been set equal to zero. The exact calculations (solid curves) are compared to results with a reduced set of eigenstates, either using 25% (dashed curves) or using 10% (dotted curves) of all eigenstates.

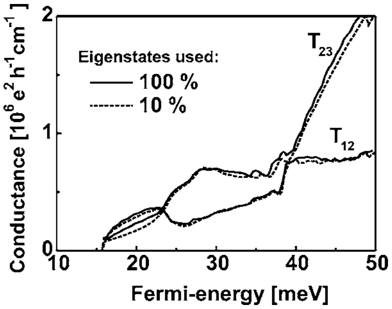

FIG. 8. The total conductance is calculated via the integration of the transmission in k space. The exact result (solid curves) is compared to the transmission obtained using only the lowest 10% of all eigenstates (dashed curves).

heterostructures with mean free paths of the order of μm has been reported.[40,41] We have calculated the differential conductance at the Fermi edge E_F between the different leads. To this end, we have integrated the transmission in k space along the $[01\bar{1}]$ direction from $k=0$ up to the Fermi wave vector. In this calculation, the Fermi levels are identical for all leads. Numerically, this is achieved by computing the transmission function for different values of $k_{[01\bar{1}]}$ from 0 to 0.1 Å^{-1}, using a homogeneous k spacing of 2×10^{-3} Å^{-1}. Figure 8 displays the resulting conductance that exhibits a highly nonmonotonic behavior. For Fermi energies below 40 meV, the calculations show that the preferred transport channel is T_{12} for Fermi energies below 24 meV. For higher energies, however, we see a switch towards the T_{23} channel. The sharp drop of the T_{12} conductance at the transition energy gives even rise to a negative differential resistance. For energies higher than 40 meV, the holes with higher energy and correspondingly larger momentum are less likely to be scattered at the junction than low energy holes which explains the larger conductance in the T_{23} channel.

The dashed lines in Fig. 8 show that the resulting conductance when only 10% of all eigenstates are taken into account. The comparison with the exact results (full lines) shows that the integrated conductance is even less sensitive to an energy cutoff that the transmission function.

D. Carrier density

The T-junction contains not only propagating states that couple to the leads with some nonzero self-energy Eq. (36), but also bound states $|b\rangle$ of energy ε_b that belong to the following subset of eigenstates $|\alpha\rangle$ of the decoupled device:

$$\varepsilon_b \in \{\varepsilon_\alpha | \Gamma^\lambda(\varepsilon_\alpha) = 0 \ \ \forall\, \lambda\}. \tag{50}$$

In a strictly ballistic calculation, these bound states would not get occupied since all of their lead self-energies are zero. In order to include these bound states, we have extended Eq. (30) for the density at grid point i,

$$n_i = \sum_{\alpha,\beta} \langle i|\alpha\rangle\langle\beta|i\rangle \xi_{\alpha\beta} + \sum_{b} \langle i|b\rangle\langle b|i\rangle f(\varepsilon_b), \tag{51}$$

where we have used the result of Appendix A for the density matrix $\Xi_{\alpha\beta}$ of a decoupled state. Note that this expression assumes all lead Fermi levels to be the same which is appropriate for the present example.

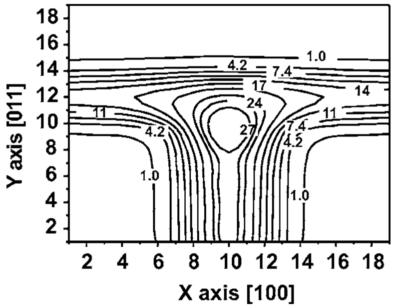

FIG. 9. Contour plot of the hole density in units of 10^{18} cm^{-3} for the T-junction at zero temperature. The Fermi level is set to 0.05 eV.

We have calculated this total local carrier density for a Fermi level of 0.05 eV at zero temperature. Note that the potential is assumed to be constant within the entire well region within the device, since this calculation is not charge self-consistent. The integrated hole density of the device is plotted in Fig. 9. It shows a high density of holes in the lower quantum well that exhibits small oscillations along the [011] axis which is due to reflections at the upper barrier. The main feature of interest is the peak in the density right at the junction which reflects a bound state. A contour plot of this laterally localized state is shown in Fig. 10. It is bound only for small values of $k_{[01\bar{1}]}$ with a binding energy of 1 meV at $k=0$.

In the calculation of this density, we have included only a fraction of the eigenstates in evaluating G^R. Since the contribution of the eigenstates to the density matrix scales with $1/(\Delta_\alpha\Delta_\beta)$, where $\Delta_{\alpha,\beta}=E-\varepsilon_{\alpha,\beta}$ according to Eq. (26), it is possible to introduce a cutoff energy E_{cutoff} that obeys the condition $E^2_{\text{cutoff}} > |(E-\varepsilon_\alpha)(E-\varepsilon_\beta)|$. For given E_{cutoff}, only states α and β are taken into account in the calculation of the density that obey this condition. The magnitude of this cutoff energy has been set to 0.1 eV which is larger than the Fermi energy of 0.05 eV. This cutoff reduces the computational effort by almost a factor of 1000. Even when we reduce the cutoff energy to 0.05 eV, the resulting density differs by less then 2% throughout the device from the one with the larger cutoff. This indicates excellent convergence of this procedure.

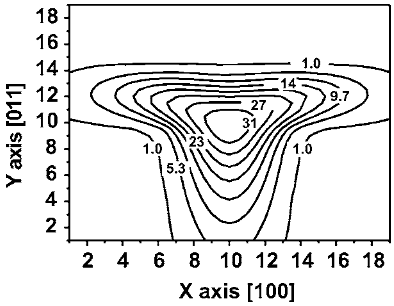

FIG. 10. Contour plot of the lateral bound state for holes. The density is given in units of 10^{17} cm^{-3}, the other parameters are the same as in the preceding figure.

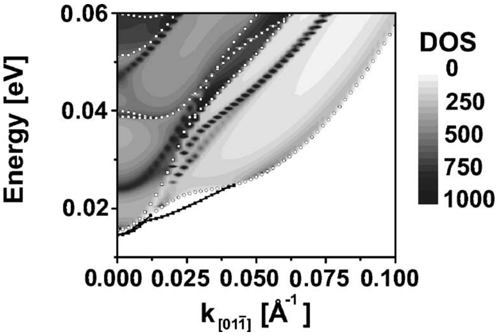

FIG. 11. The wave vector resolved density of states of the T-junction as a function of energy in eV and wave vector $k_{[01\bar{1}]}$ in units of Å^{-1}. Dark regions indicate a high density of states on a linear scale. The open circles and squares indicate the subband edges of the isolated 6 nm and 4 nm quantum wells, respectively. The solid squares depict the location of the bound states.

E. *k*-space distribution of the density of states

Further insight into the physics of this three-terminal device is obtained by studying the *k*-resolved density of states (*k*-DOS). For some device geometries, it has been shown that this property is accessible experimentally by resonant magnetotunneling spectroscopy.[42,43] In Fig. 11, the *k*-DOS is shown as a function of the energy and of the wave vector $k_{[01\bar{1}]}$ perpendicular to the device plane. The dark regions indicate high values of the *k*-DOS. Generally, this density of states possesses features that can be attributed to the individual quantum wells and others that arise from the interference between the quantum wells. The former states can be identified in Fig. 11 by the white circles and squares, respectively, which represent the subband edges of the isolated 6 nm and 4 nm quantum wells in the absence of the T-junction. The position of the two bound states is marked by solid squares in this figure; they are spin degenerate at $k_{[01\bar{1}]}=0$.

This degeneracy is lifted by the structure inversion asymmetry that splits the two states linearly proportional to k. For k values below 0.01 (1/Å), the dispersion is approximately parabolic, and we can extract the spin-splitting to be $0.07 \pm 6 \times 10^{-4}$ (eV Å). For larger values of k, the bound states eventually merge into the continuum.

This example demonstrates that the CBR method is an efficient technique to calculate the carrier density in an arbitrary shaped open device structure accurately. The main practical limitation is given by the need to take into account all lead modes in the case of multiband Hamiltonians, in contrast to the CBR method for the single-band case.

VII. ASSESSMENT OF SINGLE-BAND CBR MODE REDUCTION: RESONANT TUNNELING THROUGH A 3D QUANTUM DOT MOLECULE

To demonstrate the applicability of the CBR method to realistic 3D problems we consider a resonant tunneling diode that consists of two vertically stacked quantum dots. This structure is depicted in Fig. 12 and is composed of a 33 nm wide InP barrier layer with two embedded InAs dots that are grown on 0.5 nm thick InAs wetting layers. On both sides of the InP layer, there are thick layers of doped $In_{0.6}Ga_{0.4}As$ that act as contacts. This structure has been investigated experimentally recently.[44,45] Using the device-simulator next**nano**,[46] we have calculated the three-dimensional strain field and the corresponding piezoelectric potential. The electronic states are represented by an effective mass Hamiltonian with spatially varying masses and band offsets for the conduction band. The potential includes the strain induced deformation potential. In the present calculation, the quantum dots have been modeled by truncated pyramids of 2.5 nm height and 12 nm base width for the right dot in Fig. 12 and of 6 nm height and 16 nm base width for the left dot, respectively.

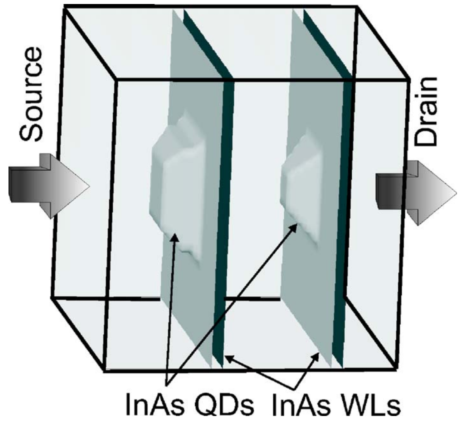

FIG. 12. The two InAs quantum dots (QDs) on top of the InAs wetting layers (WLs) are embedded within InP barrier material. The two faces in growth direction act as source and drain contacts and consist of doped $In_{0.6}Ga_{0.4}As$.

We have chosen a grid spacing of 1 nm in the two lateral directions and 0.5 nm along the propagation direction, resulting in a total number of 128 000 grid points. In spite of the large size of this device, we find the electric current to be well converged by including as few as 100 eigenstates in the computation of $\mathbf{G}^0$ in Eq. (48) and 50 propagating lead modes out of a total of 1600 modes in the relevant bias range. The calculated resonant current is shown in Fig. 13 and exhibits a very high peak-to-valley ratio in accord with the experiment. The two ground states are in resonance with one another only for a small range of voltages. The position

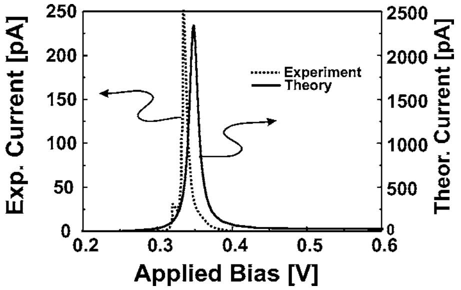

FIG. 13. Current in units of pA for the quantum dot molecule based resonant tunneling structure as a function of the applied bias in V. The scale for the experimentally observed and the calculated current is shown on the left-hand and right-hand vertical axis, respectively.

of the peak agrees very well with the experiment, whereas the maximum current and peak width exceed the measured data by one order of magnitude. Since the tunneling current depends exponentially on the barrier thickness, already small discrepancies between the assumed and the real dot shape may account for this difference, in addition to charging and scattering effects that have been ignored in these calculations.

We note that the results are well converged with respect to the lateral dimension of the structure. A more detailed description of the transport characteristics of this quantum dot molecule will be presented elsewhere.

VIII. CONCLUSION

In this work, we have shown that the electronic properties of a general two- or three-dimensional ballistic open system can be calculated efficiently in terms of a small number of eigenstates of a properly defined closed system and a few additional linear systems of small size. Any kind of open system can be arranged into an inner part of the device, contact regions, and the leads. We have shown that the Green's function formalism allows one to exploit the fact that the contact regions constitute a small fraction of the entire system very efficiently. In particular, we have found that the open device problem can be solved rigorously by breaking it down into three separate problems that can be tackled consecutively, namely a large Hermitian problem for the decoupled (closed) device, and two small non-Hermitian problems for the leads and the contacts. We have termed this method as the contact block reduction method.[28] We have shown here that this method not only applies to the transmission function,[28] but basically to any electronic observable such as the local charge density and the local density of states. As a result, this scheme avoids the repetitive solution of the entire device problem for each energy that has hampered calculations of ballistic transport for realistic devices so far.

We have shown that the CBR method is well suited to deal with multiband Hamiltonians, either in a $\mathbf{k}\cdot\mathbf{p}$ representation or in a tight-binding basis, and is applicable to devices of any shape and any number of leads in two or three spatial dimensions. The computational effort of the calculation of the transmission function and the carrier density is determined by the effort required to diagonalize the closed system's Hamiltonian. This effort can be grossly further reduced since we found that it suffices for the open system observables to include only a few percent of this Hamiltonian's eigenstates. For the special case of single-band Hamiltonians, a further significant reduction of the problem size can be achieved by transforming into the basis of all propagating lead modes. We have shown that the neglect of the decaying lead modes in the Green's function introduces only negligible errors.

As one concrete application, we have predicted the hole conductance, density, and electronic bound state in a GaAs T-junction. In addition, we have studied the ballistic transport through a resonant tunneling diode consisting of two aligned InAs quantum dots and found a single sharp resonance for tunneling between the ground states of the quantum dots, in agreement with experiment.

ACKNOWLEDGMENTS

The authors acknowledge support from the Office of Naval Research under Contract No. N00014-01-1-0242, and the Deutsche Forschungs-Gemeinschaft.

APPENDIX A: CLOSED SYSTEM LIMIT FOR THE DENSITY MATRIX EXPRESSION

In this appendix we derive an expression for the generalized density of states in Eq. (26) in the limit of the decoupled device. In this limit, the self-energy can be written as $\mathbf{\Sigma}=-i\eta\mathbf{1}$ where $\eta\rightarrow 0+$ is an infinitesimal positive constant. Correspondingly, the matrix in Eq. (10) becomes $\mathbf{\Gamma}=2\eta\mathbf{1}$, and the matrix $\mathbf{B}_C^{-1}=[\mathbf{1}-\mathbf{\Sigma}\mathbf{G}^0]^{-1}$ tends towards the unit matrix. This leads to

$$\mathbf{\Xi}_{\alpha\beta}(E)=\frac{1}{2\pi}\left(\frac{\mathrm{Tr}([|\beta\rangle\langle\alpha|]2\eta)}{(E-\varepsilon_a-i\eta)(E-\varepsilon_\beta+i\eta)}\right) \tag{A1}$$

$$=\mathrm{Tr}([|\alpha\rangle\langle\beta|])\,\delta_{\alpha\beta}\delta(E-\varepsilon_\alpha)=\delta_{\alpha\beta}\delta(E-\varepsilon_\alpha), \tag{A2}$$

where the relation

$$\lim_{\eta\rightarrow 0+}\left(\frac{1}{\pi}\frac{\eta}{(E-\varepsilon_a-i\eta)(E-\varepsilon_\beta+i\eta)}\right)=\delta_{\alpha\beta}\delta(E-\varepsilon_\alpha), \tag{A3}$$

has been used.

APPENDIX B: HAMILTONIAN FOR $\mathbf{k}\cdot\mathbf{p}$ CALCULATIONS

In our multiband example, we employ a four-band Luttinger-Kohn Hamilton represented in the $p_{3/2}$ spinor basis,[10]

$$\mathbf{H}_{kp}=\begin{bmatrix} P+Q & -S & R & 0 \\ -S^* & P-Q & 0 & R \\ R^* & 0 & P-Q & S \\ 0 & R^* & S^* & P+Q \end{bmatrix},$$

For convenience, we set $\hbar^2/(2m)=1$ in this appendix. We denote the Cartesian wave-number components along the principal axes of the crystal by k_i. Because of the orientation of the cleaved edge structure in Fig. 3, we introduce additionally the rotated components $k_y'=(k_y+k_z)/\sqrt{2}$ that lies along $[011]$, and $k_z'=(k_y-k_z)/\sqrt{2}$ along the $[01\bar{1}]$ direction. With these wave vectors, the Hamiltonian matrix elements can be written as

$$P=\gamma_1(k_x^2+k_y'^2+k_z'^2)-E_v, \tag{B1}$$

$$Q=\gamma_2\left(k_x^2-\tfrac{1}{2}k_y'^2-\tfrac{1}{2}k_z'^2+3k_y'k_z'\right), \tag{B2}$$

$$S = 2\sqrt{3}\gamma_3\left(\frac{1}{\sqrt{2}}k_y' k_x - \frac{1}{\sqrt{2}}k_z' k_x - i\frac{1}{2}(k_y'^2 - k_z'^2)\right), \tag{B3}$$

$$R = \sqrt{3}\left[-\gamma_2\left(k_x^2 - \tfrac{1}{2}k_y'^2 - \tfrac{1}{2}k_z'^2 - k_y' k_z'\right) + \sqrt{2}i\gamma_3(k_x k_y' + k_x k_z')\right]. \tag{B4}$$

Here, γ_1, γ_2, and γ_3 are the Luttinger parameters. For the discretization in real space, we quantize the x and the y axis by replacing the scalars k_x and k_y by the differentials $k_x \rightarrow -i\partial/\partial x, k_y \rightarrow -i\partial/\partial y$, whereas k_z' remains a scalar parameter. We use a finite difference mesh with constant grid spacing Δx and spatially constant Luttinger parameters $\gamma_1 = 6.98, \gamma_2 = 2.06, \gamma_3 = 2.93$. The discrete first and second order derivatives of the wave function $\psi(x,y) \rightarrow \psi_{i,j}$ can be written as

$$\frac{\partial \psi}{\partial x} = \frac{\psi_{i+1,j} - \psi_{i-1,j}}{2\Delta x}, \tag{B5}$$

$$\frac{\partial^2 \psi}{\partial x^2} = \frac{1}{\Delta x^2}(\psi_{i-1,j} - 2\psi_{i,j} + \psi_{i+1,j}), \tag{B6}$$

$$\frac{\partial^2 \psi}{\partial x\,\partial y} = \frac{1}{4\Delta x^2}(\psi_{i-1,j-1} - \psi_{i+1,j-1} - \psi_{i-1,j+1} + \psi_{i+1,j+1}). \tag{B7}$$

Correspondingly, the Hamiltonian can be divided into six Hermitian matrices as follows:

$$\mathbf{H}\left(\frac{\partial}{\partial x}, \frac{\partial}{\partial y}, k_z'\right) = \mathbf{H}_0(k_z') - i\mathbf{H}_x(k_z')\frac{\partial}{\partial x} - \mathbf{H}_{xx}\frac{\partial^2}{\partial x^2} - i\mathbf{H}_y(k_z')\frac{\partial}{\partial y} - \mathbf{H}_{yy}\frac{\partial^2}{\partial y^2} - \mathbf{H}_{xy}\frac{\partial^2}{\partial x\,\partial y}, \tag{B8}$$

$$\mathbf{H}_0(k_z') = k_z'^2\begin{bmatrix} \gamma_1 - \frac{1}{2}\gamma_2 & -i\sqrt{3}\gamma_3 & \frac{1}{2}\sqrt{3}\gamma_2 & 0 \\ & \gamma_1 + \frac{1}{2}\gamma_2 & 0 & \frac{1}{2}\sqrt{3}\gamma_2 \\ & & \gamma_1 + \frac{1}{2}\gamma_2 & i\sqrt{3}\gamma_3 \\ & & & \gamma_1 - \frac{1}{2}\gamma_2 \end{bmatrix}, \tag{B9}$$

$$\mathbf{H}_x(k_z) = k_z'\begin{bmatrix} 0 & \sqrt{6}\gamma_3 & \sqrt{6}i\gamma_3 & 0 \\ & 0 & 0 & \sqrt{6}i\gamma_3 \\ & & 0 & -\sqrt{6}\gamma_3 \\ & & & 0 \end{bmatrix}, \tag{B10}$$

$$\mathbf{H}_{xx} = \begin{bmatrix} \gamma_1 + \gamma_2 & 0 & -\sqrt{3}\gamma_2 & 0 \\ & \gamma_1 - \gamma_2 & 0 & -\sqrt{3}\gamma_2 \\ & & \gamma_1 - \gamma_2 & 0 \\ & & & \gamma_1 + \gamma_2 \end{bmatrix}, \tag{B11}$$

$$\mathbf{H}_y(k_z) = k_z'\begin{bmatrix} 3\gamma_2 & 0 & \sqrt{3}\gamma_2 & 0 \\ & -3\gamma_2 & 0 & \sqrt{3}\gamma_2 \\ & & -3\gamma_2 & 0 \\ & & & 3\gamma_2 \end{bmatrix}, \tag{B12}$$

$$\mathbf{H}_{yy} = \begin{bmatrix} \gamma_1 - \frac{1}{2}\gamma_2 & i\sqrt{3}\gamma_3 & \frac{1}{2}\sqrt{3}\gamma_2 & 0 \\ & \gamma_1 + \frac{1}{2}\gamma_2 & 0 & \frac{1}{2}\sqrt{3}\gamma_2 \\ & & \gamma_1 + \frac{1}{2}\gamma_2 & -i\sqrt{3}\gamma_3 \\ & & & \gamma_1 - \frac{1}{2}\gamma_2 \end{bmatrix}, \tag{B13}$$

$$\mathbf{H}_{xy} = \begin{bmatrix} 0 & -\sqrt{6}\gamma_3 & i\sqrt{6}\gamma_3 & 0 \\ & 0 & 0 & i\sqrt{6}\gamma_3 \\ & & 0 & \sqrt{6}\gamma_3 \\ & & & 0 \end{bmatrix}. \tag{B14}$$

APPENDIX C: MODE SPACE GREEN'S FUNCTION: AN ANALYTICAL MODEL

In this appendix, we analyze the Green's function of the simple 2D device depicted in the inset of Fig. 2 analytically. In contrast to the numerical studies that are based on a discretization of real space, here we employ a continuum real space representation of the Schrödinger equation. For $W_L \geqslant W_D$, both the lead states and the states of the decoupled device are separable in coordinate space. The wire modes are product states of one-dimensional plane waves along the vertical z direction and confined modes along the lateral y direction. The wire dispersion $k_l(E)$ at energy E inside the leads $\lambda = 1,2$ follows from

$$k_{l_\lambda} = \pm\sqrt{\frac{2m^*}{\hbar^2}(E - \varepsilon_{l_\lambda})},$$

$$\varepsilon_{l_\lambda} = \frac{\hbar^2\pi^2}{2m^* W_L^2}l_\lambda^2, \tag{C1}$$

where $l_\lambda = 1,2,\ldots$. The decoupled device is characterized by the Hermitian Hamiltonian H^N that obeys von Neumann boundary conditions at the contacts and Dirichlet boundary conditions everywhere else. Its eigenstates are product states of lateral confined modes along the y direction (labeled by $\|$) and vertically confined modes along the z axis (labeled by $\perp$). The eigenvalues of the decoupled device are given by

$$E_{n_\perp n_\|} = E_{n_\perp} + E_{n_\|} \equiv E_\perp n_\perp^2 + E_\| n_\|^2 \tag{C2}$$

$$= \frac{\hbar^2\pi^2}{2m^* L^2}n_\perp^2 + \frac{\hbar^2\pi^2}{2m^* W_D^2}n_\|^2, \tag{C3}$$

where $n_\perp = 0,1,2,\ldots$ and $n_\| = 1,2,\ldots$. After some algebra, the matrix elements of G^0 in the left contact region, expressed in terms of the lead modes $l_1, l_2 = 1,\ldots,M$, can be written

$$\langle l_1 z=0|G^0|l_2 z=0\rangle = P_{\rm odd}\sum_{n_\parallel}^{\rm odd} M(l_1,l_2,n_\parallel)V(E,n_\parallel) + P_{\rm even}\sum_{n_\parallel}^{\rm even} M(l_1,l_2,n_\parallel)V(E,n_\parallel), \tag{C4}$$

$$P_{\rm odd} = \frac{16r}{L\pi^2}\cos\left(\frac{W_D l_1 \pi}{2W_L}\right)\sin\left(\frac{l_1\pi}{2}\right)\cos\left(\frac{W_D l_2 \pi}{2W_L}\right)\sin\left(\frac{l_2\pi}{2}\right),$$

$$P_{\rm even} = \frac{16r}{L\pi^2}\sin\left(\frac{W_D l_1 \pi}{2W_L}\right)\cos\left(\frac{l_1\pi}{2}\right)\sin\left(\frac{W_D l_2 \pi}{2W_L}\right)\times\cos\left(\frac{l_2\pi}{2}\right),$$

$$M(l_1,l_2,n_\parallel) = \frac{E_{n_\parallel}}{(\varepsilon_{l_1}-E_{n_\parallel})(\varepsilon_{l_2}-E_{n_\parallel})}, \tag{C5}$$

$$V(E,n_\parallel) = \frac{\pi}{E_\perp}\frac{\cot(\sqrt{R}\pi)}{\sqrt{R}}, \quad R = \frac{E-E_{n_\parallel}}{E_\perp}. \tag{C6}$$

There are two factors in this expression that ensure convergence for given energy E. The factor V ensures exponential convergence as a function of $n_\parallel$ because it tends to zero exponentially for nonpropagating device modes with $E_{n_\parallel} > E$. Indeed, for $R < 0$ we have $V \propto \coth(\sqrt{|R|}\pi)/\sqrt{|R|} \to 0$ for $R \to -\infty$. This result is a consequence of the chosen von Neumann boundary conditions of the decoupled device. *This explains why it suffices to calculate the decoupled device's Green's function with a small number of device eigenstates.*

The factor M, on the other hand, expresses lateral wave vector matching. Obviously, this factor attains a maximum for lead energies $\varepsilon_l \approx E_{n_\parallel}$ with the influence of other modes decreasing quadratically. Since only the propagating device modes $E_{n_\parallel} < E$ contribute significantly to the matrix element of G^0 as we have just seen, the same result holds for the lead modes which explains why only a few modes need to be taken into account in calculating G^0. Finally, the prefactors $P_{\rm odd}, P_{\rm even}$ are geometry dependent terms. Note that they vanish for $W_D = W_L$ and $l \neq n_\parallel$ which expresses exact lateral momentum conservation in this limiting case.

In order to show that the arguments for mode reduction also apply to the full G^R of the open device, we note that the self-energy Eq. (46) reads in lead mode space

$$\langle l_\lambda z_\lambda|\Sigma_\lambda|l_\lambda z_\lambda\rangle = -\frac{i}{2}\frac{\hbar^2 k_{l_\lambda}}{m^*}, \tag{C7}$$

which is not small and actually increases linearly with l_λ for $l_\lambda \to \infty$. However, since G^0 decreases quadratically with l, the products $(G_C^0 \Sigma_C G_C^0)_{ll'}$ and higher order terms are also convergent quadratically in the outermost mode indices l, l'.

---

[1] R. Landauer, Phys. Scr., T, **T42**, 110 (1992).
[2] M. Büttiker, IBM J. Res. Dev. **32**, 317 (1988).
[3] E. O. Kane, in *Tunneling Phenomena in Solids*, edited by E. Burstein and S. Lundqvist (Plenum, New York, 1969), p. 1.
[4] J. N. Schulman and Y. C. Chang, Phys. Rev. B **27**, 2346 (1983).
[5] C. Mailhiot and D. L. Smith, Phys. Rev. B **33**, 8360 (1986).
[6] W. Frensley, Rev. Mod. Phys. **62**, 745 (1990).
[7] http://www.utdallas.edu/~frensley/technical%/qtrans/qtrans.html
[8] C. Lent and D. Kirkner, J. Appl. Phys. **67**, 6353 (1990).
[9] D. Z. Y. Ting, E. T. Yu, and T. C. McGill, Phys. Rev. B **45**, 3583 (1992).
[10] Y. X. Liu, D. Z. Y. Ting, and T. C. McGill, Phys. Rev. B **54**, 5675 (1996).
[11] E. S. Daniel, X. Cartoixa, W. Frensley, D. Z.-Y. Ting, and T. C. McGill, IEEE Trans. Electron Devices **47**, 1052 (2000).
[12] C. Strahberger and P. Vogl, Phys. Rev. B **62**, 7289 (2000).
[13] E. Polizzi and N. BenAbdallah, J. Appl. Phys. **87**, 8700 (2000).
[14] E. Polizzi and N. BenAbdallah, Phys. Rev. B **66**, 245301 (2002).
[15] P. A. Ramachandran, *Boundary Element Methods in Transport Phenomena* (WIT Press, Southampton, UK, 1993).
[16] H. Frohne, M. McLennan, and S. Datta, J. Appl. Phys. **66**, 2699 (1989).
[17] P. A. Knipp and T. L. Reinecke, Phys. Rev. B **54**, 1880 (1996).
[18] D. K. Ferry and S. M. Goodnick, *Transport in Nanostructures* (Cambridge University Press, Cambridge, UK, New York, 1997).
[19] R. Lake, G. Klimeck, R. C. Bowen, and D. Jovanovic, J. Appl. Phys. **81**, 7845 (1997).
[20] A. Svizhenko, M. P. Anantram, T. R. Govindan, B. Biegel, and R. Venvgopal, J. Appl. Phys. **91**, 2343 (2002).
[21] R. Venugopal, Z. Ren, S. Datta, and M. S. Lundstrom, and D. Jovanovic, J. Appl. Phys. **92**, 3730 (2002).
[22] C. Rivas and R. Lake, Phys. Status Solidi B **239**, 94 (2003).
[23] S. Rotter, J. Z. Tang, L. Wirtz, J. Trost, and J. Burgdörfer, Phys. Rev. B **62**, 1950 (2000).
[24] S. Rotter, B. Weingartner, N. Rohringer, and J. Burgdörfer, Phys. Rev. B **68**,165302 (2003).
[25] S. E. Laux, A. Kumar, and M. V. Fischetti, J. Appl. Phys. **95**, 5545 (2004).
[26] Supriyo Datta, *Electronic Transport in Mesoscopic Systems* (Cambridge University Press, Cambridge, 1995).
[27] Supriyo Datta, Superlattices Microstruct. **28**, 253 (2000).
[28] D. Mamaluy, M. Sabathil, and P. Vogl, J. Appl. Phys. **93**, 4628 (2003).
[29] In the single band case, the matrix $\mathbf{B}_C$ reduces to $\mathbf{A}_C^T$.
[30] Y. Meir and N. S. Wingreen, Phys. Rev. Lett. **68**, 2512 (1992).
[31] P. S. Krstic, X. G. Zhang, and W. H. Butler, Phys. Rev. B **66**, 205319 (2002).
[32] G. Schedelbeck, W. Wegscheider, M. Bichler, and G. Abstreiter, Science **278**, 1792 (1997).
[33] A. Yacoby, H. L. Stormer, N. S. Wingreen, L. N. Pfeiffer, K. W. Baldwin, and K. W. West, Phys. Rev. Lett. **77** 4612 (1996).
[34] H. Akiyama, T. Someya, and H. Sakaki, Phys. Rev. B **53**, R4229 (1996).

[35] H. Akiyama, J. Phys.: Condens. Matter **10**, 3095 (1998).

[36] R. de Picciotto, H. L. Störmer, A. Yacobi, K. W. Baldwin, L. N. Pfeiffer, and K. W. West, Physica E (Amsterdam) **6**, 514 (2000).

[37] F. Ertl, T. Asperger, R. A. Deutschmann, W. Wegscheider, M. Bichler, G. Bohm, and G. Abstreiter, Physica E (Amsterdam) **13**, 920 (2002).

[38] J. Höntschel, R. Stenzel, W. Klix, F. Ertl, T. Asperger, R. A. Deutschmann, M. Bichler, and G. Abstreiter, in *Simulation of Semiconductor Processes and Devices 2001*, Springer Conference Proceedings, edited by D. Tsoukalas, and C. Tsamis (Springer, Berlin, 2001), p.222.

[39] D. Boese, M. Governale, A. Rosch, and U. Zülicke, Physica E (Amsterdam) **12**, 730 (2002).

[40] D. Sprinzak, M. Heiblum, Y. Levinson, and Hadas Shtrikman, Phys. Rev. B **55**, R10185 (1997).

[41] J. P. Lu, J. B. Yau, S. P. Shukla, M. Shayegan, L. Wissinger, U. Rössler, and R. Winkler, Phys. Rev. Lett. **81**, 1282 (1998).

[42] R. K. Hayden, D. K. Maude, L. Eaves, E. C. Valadares, M. Henini, F. W. Sheard, O. H. Hughes, J. C. Portal, and L. Cury, Phys. Rev. Lett. **66**, 1749 (1991).

[43] R. R. Marquardt, D. A. Collins, Y. X. Liu, D. Z. Y. Ting, and T. C. McGill, Phys. Rev. B **53**, 13624 (1996).

[44] M. Borgstrom, T. Bryllert, T. Sass, B. Gustafson, L. E. Wernersson, W. Seifert, and L. Samuelson, Appl. Phys. Lett. **78**, 3232 (2001).

[45] T. Bryllert, M. Borgstrom, T. Sass, B. Gustafson, L. Landin, L. E. Wernersson, W. Seifert, and L. Samuelson, Appl. Phys. Lett. **80**, 2681 (2002).

[46] http://www.wsi.tum.de/nextnano3/